Upgrade of the magnetic diagnostic system for restart of HT-6M operation

Li-Xing Chen(陈力行)[1,2], Biao Shen(沈飙)[1], Da-Long Chen(陈大龙)[1,†], Zheng-Ping Luo(罗正平)[1,‡], Zu-Chao Zhang(张祖超)[1], Ying Chen(陈颖)[1], Yong Wang(王勇)[1], and Jin-Ping Qian(钱金平)[1]

[1] *Institute of Plasma Physics, Hefei Institutes of Physical Science, Chinese Academy of Sciences, Hefei* 230026, *China*
[2] *University of Science and Technology of China, Hefei* 230026, *China*

(Received 30 May 2022; revised manuscript received 4 July 2022; accepted manuscript online 8 July 2022)

The HT-6M tokamak at the Thailand Institute of Nuclear Technology has been restarted. In order to ensure the smooth breakdown of plasma and obtain plasma discharge parameters, optimization of the poloidal field coils and upgrade of the magnetic diagnostics are described in this article. A perfect null field (stray field in the main chamber < 10 G) is obtained using an ohmic heating field. To obtain important information about the plasma, an external magnetic diagnostics system is designed and calibrated, including a Rogowski coil (measuring plasma current), a magnetic probe (measuring external field), diamagnetic loops (measuring β_p) and so on. In order to realize high-frequency signal measurement and transmission, a series of frequency responses with the magnetic probe and transmission line are tested. Later, to verify the null field, a fitting code is developed to reconstruct the stray field in the vacuum chamber based on magnetic probe measurements and flux loops. The results show that the error is within 1.5%. This indicates the accuracy of the magnetic measurement system and ensures the preparation for the breakdown of plasma.

Keywords: HT-6M, null field, magnetic measurement, high frequency calibration

PACS: 52.55.Fa, 52.70.Ds, 52.80.Pi **DOI:** 10.1088/1674-1056/ac7f93

1. Introduction

In tokamak plasma experiments, a sufficient area of null field in the center of the chamber is necessary for plasma breakdown,[1] since the gas (such as hydrogen or deuterium) in the center can be easily broken down by the loop voltage, giving rise to an avalanche effect before it touches the wall. Once a tokamak plasma has been generated and sustained, a pair of vertical fields is generated to control horizontal displacement of the plasma,[2] due to the nonuniformity of the toroidal field. To directly measure information on the discharge operation, a series of magnetic probes,[3] based on Maxwell's law, can provide key plasma parameters such as plasma current,[4] magnetic field, loop voltage, poloidal beta and flux loop.[5] These magnetic sensors, measuring plasma current and magnetic field, are used for plasma equilibrium reconstruction.[6–8] A Mirnov coil is used for magnetohydrodynamic (MHD) detection and physics analysis.[9]

HT-6M (1984–2002), was developed at the Institute of Plasma Physics, Hefei Institute of Physical Science. It is a small tokamak ($R = 0.65$ m, $a = 0.20$ m) with a circular plasma configuration. In 2021, HT-6M was restarted to provide education and scientific research for the Thailand Institute of Nuclear Technology. Under the current plasma parameters, based on the electromagnetic diagnostics system, the tokamak can be used to carry out some basic plasma research, such as plasma breakdown, ramp-up, formation and ramp down. Furthermore, due to the shift of plasma in the R direction, HT-6M can use a magnetic probe to detect horizontal displacement of the plasma and do some corresponding displacement control experiments. As for MHD physics, the tearing mode (10 kHz–50 kHz) will be observed during the ohmic discharge. Since the device has been decommissioned for 20 years, the position of the ohmic heating coils has changed a lot and could not provide the necessary null field. All the magnetic sensors were replaced. To restart experiments on the device, optimization of coil positions and upgrade of the magnetic diagnostics were necessary.

The organization of this article is as follows. Section 2 discusses the design of the coil optimization for a perfect null field. Section 3 discusses the design of each inductive sensor, for example Rogowski loops,[10] flux loops, magnetic probes,[11] and diamagnetic loops.[12,13] Section 4 describes the calibration and experimental results of the magnetic sensors.

2. Optimization of the ohmic heating field

Figure 1 shows the structure of HT-6M. The poloidal field (PF) coils are used to break down, drive and balance the plasma for the following plasma discharge experiments. Based on its function, there are two independent types of PF coil. One is the ohmic heating field (OHF) coil and the second is the vertical field (VF) coil. In the device, OHF coils are first used to break down the plasma, then drive the plasma

†Corresponding author. E-mail: cdalong@ipp.ac.cn
‡Corresponding author. E-mail: zhpluo@ipp.ac.cn

© 2022 Chinese Physical Society and IOP Publishing Ltd

current for as long as the flux swing can heat the plasma. The OHF coils also provide a perfect null field (the stray field in main chamber < 10 G) by the center solenoid (CS; OHF1) coils and its compensation coils (OHF2U, OHF2L, OHF3U and OHF3L). The VF coils (VF1 and VF2) are designed to control the plasma position to avoid horizontal displacement.

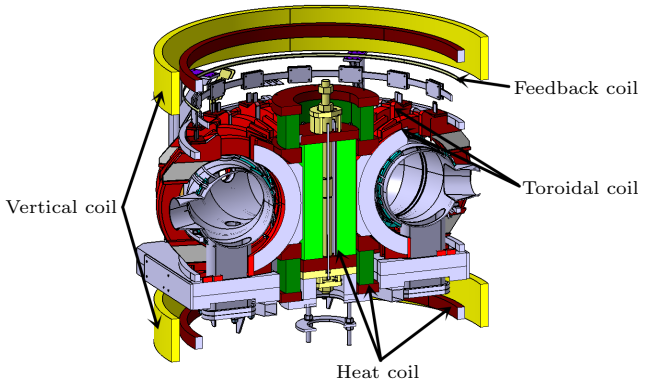


Fig. 1. The design structure of HT-6M.

Based on the parameters of the OHF before optimization and the calculated Green's function[14] between the OHF coils and the plasma grids covering the whole vacuum vessel, the flux distribution and poloidal field due to the OHF coils can be calculated. Since the device had been in storage for a long time the poloidal field position had moved. According to the calculations, the stray field in the torus is larger than 100 G, which will be unfavorable to plasma breakdown in the future (seen in Fig. 2(a)). In order to have an optimized null field for the upgraded HT-6M, a large region with small stray field in the chamber can be obtained after adjusting the position of the OHF coils. Since the CS coil (OHF1) will provide most of the heating flux, its parameters will be kept fixed. Then the compensation coils can be optimized to enlarge the null field region (Table 1). Meanwhile, the R coordinate of these compensation coils is fixed to keep them coaxial, and these are not allowed to change here. Then, the only way to have an optimized null field region is to adjust their Z coordinates. As shown in Fig. 2, the desired null field region is defined by a series of discrete points (the blue points in the vacuum chamber; Fig. 2(b)). The allowed optimal ranges for movement of OHF2U/L and OHF3U/L are defined (blue dot dash lines). An optimization procedure calculates the vertical component of the poloidal field ($B_{z,\mathrm{pts}}$) at the discrete points to be 1 G ($B^{\mathrm{tgt}}_{z,\mathrm{pts}} = 1$ G) when moving the compensation coils OHF2U/L and OHF3U/L. Once the cost function

$$\zeta = \sum_{i=1}^{n_{\mathrm{pt}}} \left(B^{\mathrm{cal}}_{z,\mathrm{pts}} - B^{\mathrm{tgt}}_{z,\mathrm{pts}} \right)^2 \tag{1}$$

has a minimum value, $\min \zeta$, the optimized positions (Z coordinates) for OHF2U/L and OHF3U/L are obtained. In above equation, $B^{\mathrm{cal}}_{z,\mathrm{pts}}$ is the calculated poloidal field on the desired null field region points and n_{pt} is the number of chosen points.

The optimized null field can be reached after adjusting the compensated coils. Figure 2(c) shows that a large region with a small stray field (< 10 G) can be reached with the optimized OHF coils, as shown in Table 1. The coordinate before optimization is Z_{b} and after optimization it is Z_{c}.

Table 1. OHF coil parameters of the upgraded HT-6M.

	OHF1	OHF2U	OHF2L	OHF3U	OHF3L
R_{in} (mm)	84.8	225	225	897.5	897.5
R_{out} (mm)	195.2	315	315	947.6	947.6
Z_{b} (mm)	0.0	498.5	−498.5	721	−721
Z_{c} (mm)	0	510	−510	860	−860
ΔZ (mm)	740	225	225	80	80
Turn_R	6	4	4	3	3
Turn_Z	30	7	7	2	2

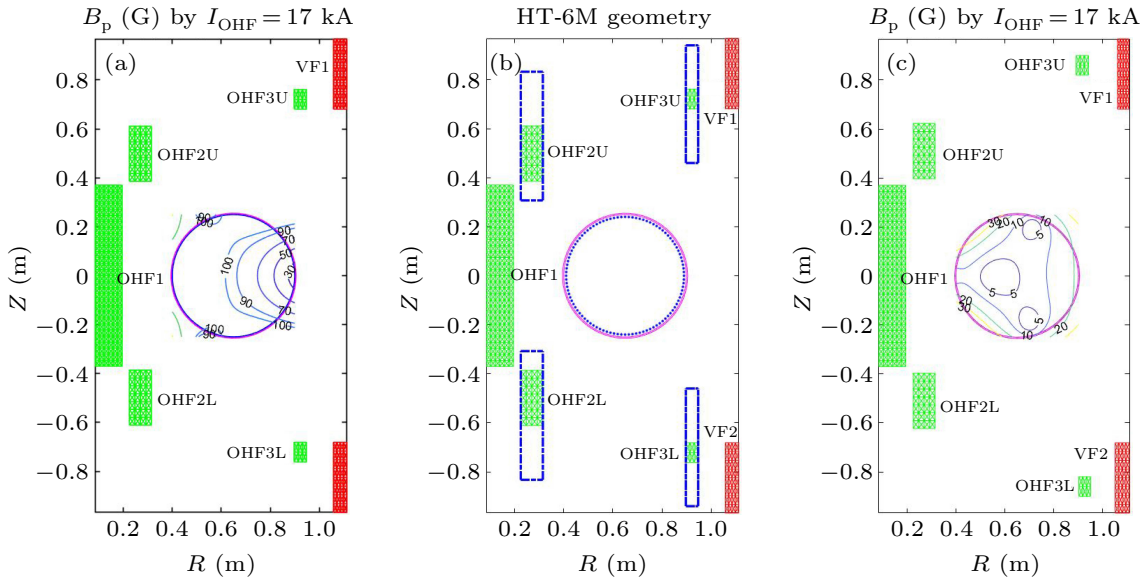


Fig. 2. Position of the ohmic heating field (OHF) and poloidal field distribution. (a) Poloidal field distribution due to OHF coils ($I_{\mathrm{OHF}} = 17$ kA) before optimization. (b) Schematic of OHF coil optimization. (c) Poloidal field distribution by OHF coils ($I_{\mathrm{OHF}} = 17$ kA) in a small region < 10 G.

3. Design of the magnetic sensors

In this section we discuss the design of the magnetic sensors. Table 2 shows the parameters of HT-6M during operation. Figure 3 shows the electromagnetic probe distribution. Each inductive sensor consists of a conducting loop or coil, Rogowski loops, flux loops, magnetic probes and diamagnetic loops; details are described in the following.

Table 2. HT-6M device parameters.

Name	Function	Value
Rogowski coil	plasma current	0–150 kA
	OH current	0–17 kA
	TF current	0–8 kA
	VF current	0–5 kA
	feedback control	0–300 A
Mirnov/magnetic coil	poloidal magnetic field	
	m,n-MHD	$m<6, n<8$
Flux loops	toroidal voltage	0.7 V·s
	poloidal flux	
Diamagnetic loops	plasma energy, β_p	

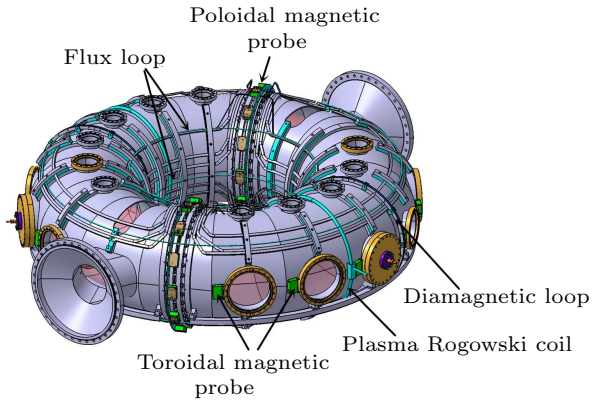


Fig. 3. Diagram of the electromagnetic probe distribution.

3.1. Rogowski loops

In HT-6M, in order to measure the toroidal field current, ohmic field current, vertical field current, feedback field current and plasma current, respectively, five pairs of Rogowski coils are installed in the current circuit, according to the device parameters.

A Rogowski coil is an effective tool for measuring instantaneous current.[10] After uniformly and closely winding the skeleton with N turns, the changing current will induce a changing magnetic flux in the skeleton, and the changing magnetic flux will generate an induced electromotive force at the end of the coil. Combined with the Ampère loop law and Faraday's law of electromagnetic induction, the measured voltage is given by

$$V = \int \varepsilon \,\mathrm{d}t = \int M \,\mathrm{d}i_\mathrm{t} = MI = -\mu_0 ns \cdot i_\mathrm{t}, \tag{2}$$

where i_t is the current to be measured, s is the cross-sectional area of the Rogowski coil, n is the winding density, which is the number of winding turns per unit length, and M is the mutual inductance estimated from S and n. As shown in the formula, the cross-sectional area and winding density of a Rogowski coil directly determine the signal quality.

Since the vacuum chamber of a tokamak needs to be baked at 200 °C, the Rogowski coil used to measure plasma current is made of materials that are resistant to high temperatures. The winding fiber inside the coil is made of high temperature resistant enameled wire. The protective sleeve of the outer layer of the coil is made of silica gel. The other Rogowski coils have no special requirements. The mutual inductance coefficients L of the plasma current coil, PF and TF coils are all 2.71×10^{-7} H.

To obtain the real physical current the detector circuit is equipped with a self-triggered integrator. A better sensitivity can be obtained by changing the integral constant. In this diagnostic system, the RC constants of the plasma current Rogowski coil, the ohmic current Rogowski coil, the toroidal Rogowski coil, the vertical current Rogowski coil and the feedback current Rogowski coil are 3.88 ms, 0.533 ms, 0.247 ms, 0.152 ms, and 0.028 ms, respectively.

The plasma current Rogowski coils are toroidally arranged at 0° and 180°. The toroidal field, ohmic field, vertical field and HDF field Rogowski coils are arranged around the power bus-line.

3.2. Flux loops

To obtain the loop voltage and measure the horizontal and vertical displacement of the plasma, the flux loops are designed and installed outside HT-6M's vacuum vessel. The flux loop, arranged on one ring, measures the toroidal loop voltage and poloidal flux loop. The loop voltage can be used for plasma breakdown and for evaluation of plasma discharge parameters. The magnetic flux mainly comes from the plasma current

$$\psi = B_\mathrm{PF} \cdot S_\mathrm{FL}, \tag{3}$$

where B_PF is the poloidal field and S_FL is area of the flux loop. Later in the discharge, when the poloidal field current tends to be stable, the loop voltage mainly come from the plasma,[15]

$$U_\mathrm{L} = R_\mathrm{P} I_\mathrm{P} + L_\mathrm{P} \frac{\mathrm{d}I_\mathrm{P}}{\mathrm{d}t}, \tag{4}$$

where I_P is the plasma loop current, L_P is the plasma loop inductance and R_P is the plasma loop resistance. R_P can be expressed as

$$R_\mathrm{P} = 2\pi R \left(\int_s \sigma \,\mathrm{d}s \right)^{-1}, \tag{5}$$

where R is the plasma large radius, S is the plasma cross-section area and σ is the parallel conductivity divided by the effective charge number.

To obtain the horizontal and vertical displacement of the plasma, the flux loops are installed on the high-field side

$(\psi(\rho,\pm\frac{3\pi}{4}))$ and lower-field side $(\psi(\rho,\pm\frac{\pi}{4}))$, as shown in Fig. 4. The plasma horizontal displacement[16] is given by

$$\frac{\left[\psi\left(\rho,\frac{\pi}{4}\right)+\psi\left(\rho,-\frac{\pi}{4}\right)-\psi\left(\rho,\frac{3\pi}{4}\right)-\psi\left(\rho,-\frac{3\pi}{4}\right)\right]}{\frac{\sqrt{2}\mu_0 I_{\mathrm{P}} R_0}{\pi\rho}} = \Delta_{\parallel}-\Delta_0, \tag{6}$$

and the plasma vertical displacement by

$$\frac{\left[\psi\left(\rho,\frac{\pi}{4}\right)-\psi\left(\rho,-\frac{\pi}{4}\right)+\psi\left(\rho,\frac{3\pi}{4}\right)-\psi\left(\rho,-\frac{3\pi}{4}\right)\right]}{\frac{\sqrt{2}\mu_0 I_{\mathrm{P}} R_0}{\pi\rho}} = -\Delta_{\perp}, \tag{7}$$

where $\psi(\rho,\theta)$ is the plasma magnetic flux, ρ is the position in the R direction, θ is the probe angle, $\Delta_{\parallel}$ is the plasma horizontal displacement, Δ_0 is the correction introduced by the toroidal plasma current, μ_0 is the permeability of a vacuum, I_{P} is the plasma current and R_0 is the distance from the probe to the geometric center.

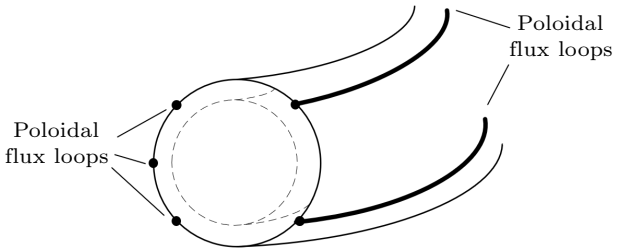


Fig. 4. Poloidal flux loop installation diagram.

The flux loops measuring the loop voltage are installed on the middle plane in the high-field side. So as not to be damaged by the high baking temperature, the flux loops are made of polyether ether ketone (PEEK) cable and are fixed inside a stainless steel tube. Since the induced voltage from the flux loop is so high, the matched RC value of the integrator is 200 ms.

3.3. Magnetic probes

To measure the magnetic field and MHD issues (such as m/n mode or mode frequency), the upgraded magnetic probes are usually arranged around the poloidal and toroidal directions of the plasma. According to the law of electromagnetic induction, when a coil in a magnetic field induces a certain voltage, the signal can be integrated to obtain the flux value through the coil region. The magnetic flux can be treated as the magnetic field value with a smaller coil volume than the entire observation space. The formulae are as follows:[11,19]

$$\varepsilon = -\frac{\mathrm{d}\boldsymbol{B}}{\mathrm{d}t}\cdot N\cdot S, \tag{8}$$

$$\int \varepsilon\,\mathrm{d}t = -\int \mathrm{d}\boldsymbol{B}\cdot N\cdot S, \tag{9}$$

$$\varepsilon = -\boldsymbol{B}\cdot N\cdot S\cdot\frac{G}{R\cdot C},\quad (G=1), \tag{10}$$

$$\boldsymbol{B} = -\varepsilon\times k,\quad \left(k=\frac{R\cdot C}{N\cdot S}\right), \tag{11}$$

where $\boldsymbol{B}$ is the magnetic field as measured by the probe, ε is the output voltage, N is the magnetic probe winding number, S is the induced area of the probe in one turn, R is the equivalent resistance of the integrator, C is the equivalent capacitance of the integrator, NS is the effective induced area and RC is the integrator constant.

The magnetic probes are installed in two arrays in different toroidal positions with 180° symmetry. Each array has 12 probes in the poloidal plane. They are used to measure the poloidal field and m-mode. Sixteen probes arranged in the low-field side and in the equatorial plane are used to measure the n-mode.

A larger probe's effective induced area (NS value) will lead to a higher output amplitude. However, due to space restrictions between the vacuum vessel and toroidal field coils, the probe height space is less than 35 mm. Based on experience with tokamak operation, to obtain a high-quality output signal, the NS value of the magnetic probes should be larger than 0.1 m^2. Finally, the length, width and height of the probe are 36 mm, 36 mm, and 20 mm, respectively. The number of turns of the coil in both directions is eight and the corresponding active area NS ranges between 0.12 m^2 and 0.32 m^2. The coil is designed in two dimensions to measure tangential and radial field simultaneously. The tangential field direction measures the polar direction and the radial field direction measures the normal direction. The tangential field and the radial field, respectively, adopt integral constant integrators of 5 ms and 10 ms.

Since the vacuum chamber of the tokamak needs to be baked at 200 °C, the magnetic probes are made of PEEK and the wires of polyimide enameled wire. These materials have a high melting point. Specific design and installation drawings are shown in Fig. 5.

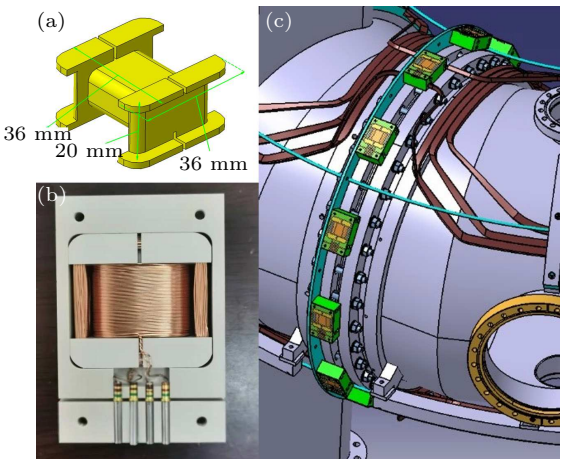


Fig. 5. Magnetic probe: (a) diagram of the probe design diagram, (b) photograph of the magnetic field probe, (c) installation position of the polar probe.

3.4. Diamagnetic loops

To evaluate the performance of magnetic confined plasmas and measure poloidal beta (β_p), measurement of the diamagnetic flux is achieved by the diamagnetic loops, which consist of one compensation loop excluding the plasma column and two concentric poloidal loops enclosing the plasma column.

The diamagnetic coil is a multi-turn coil around the plasma circular flux. It can diagnose changes in the toroidal flux which are associated with transverse thermal motion of the plasma.

Since the diamagnetic signal is only 10^{-3}–10^{-4} times the toroidal field flux, the diamagnetic compensation measurement system is composed of a diamagnetic coil and a compensation coil, the designs of which are shown in Fig. 6. The system uses the compensation coil signal to compensate the toroidal field signal, which is also measured by the diamagnetic coil, remove the stray signal and obtain the real diamagnetic signal.[12,13]

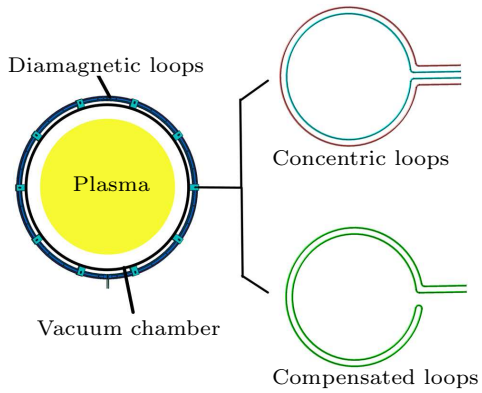


Fig. 6. Design of the diamagnetic loops.

The flux linked to the inner loop during a plasma discharge can be expressed as

$$\Phi_I = (\Phi_I)_{PF} + (\Phi_I)_{TF} + (\Phi_I)_w + \Phi_{dia}, \tag{12}$$

where Φ_I is the inner coil total flux, $(\Phi_I)_{PF}$ is the flux contributed by the ohmic field and vertical field and $(\Phi_I)_{TF}$ is the flux contributed by toroidal field. Since the poloidal field is theoretically perpendicular to the inner loop, the flux contribution from the PF coil is very small compared with that from the TF coil. Φ_{dia} is the flux contributed by the plasma. $(\Phi_I)_w$ is very complicated, as the changed toroidal field will induce a poloidal wall current, giving an extra toroidal flux contribution. This motivated us to add a compensation loop

$$\Phi_c = (\Phi_c)_{PF} + (\Phi_c)_{TF} + (\Phi_c)_w, \tag{13}$$

where Φ_c is the compensation loop total flux, $(\Phi_c)_{PF}$ is the flux contribution from the poloidal field, $(\Phi_c)_{TF}$ is the flux contribution from the toroidal field and $(\Phi_c)_w$ is the flux from the wall current.

The inner flux loop and compensation loop are installed in the same plane, so Φ_I can be simplified as

$$\Phi_I = k \times \Phi_c + \Phi_{dia}, \tag{14}$$

where $k = S_I/S_c$, S_I is the area of the inner coil and S_c is the area of the compensation loop. In the experiment to check the coefficient k, a series of vacuum shots with TF current will be performed. In HT-6M, the diamagnetic loops have two loops, and the compensation loops have one loop.

4. Calibration of magnetic sensors and experimental results

Calibration of the magnetic sensor system is necessary if we are to obtain actual and accurate physical values for a plasma, such as poloidal field and current. In this section we describe calibration of the magnetic sensors, including *NS* value measurement, frequency response calibration, Rogowski coil testing and *RC* value calibration. Magnetic sensor experiments with pure poloidal current are described.

4.1. Calibration of magnetic sensors

The *NS* value calibration The *NS* calibration system is tested on a long and straight solenoid. An alternating and uniform magnetic field is generated in the induction area calibration system.[19] The calibration error can reach less than one part in a thousand, and simultaneous calibration of multiple probe coils can be realized. The specific operation block diagram is shown in the Fig. 7.

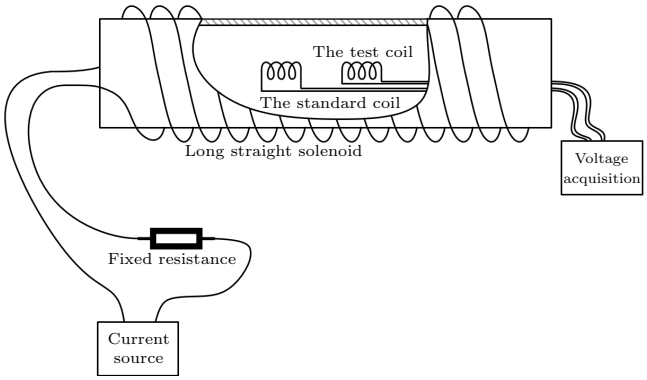


Fig. 7. System block diagram for *NS* value calibration.

Frequency response calibration Due to the special requirements for the discharge parameters of the upgraded HT-6M device, calibration of the frequency response, including amplitude–frequency and phase–frequency calibration, are tested, as shown in Fig. 8(a). The fixing fixture of the probe coil is placed in the Helmholtz coil, so that the probe coil is fixed in the center of the Helmholtz coil. The frequency response bandwidth of the probe is 140 kHz for the inner ring and 120 kHz for the outer ring, which meet operational requirements.

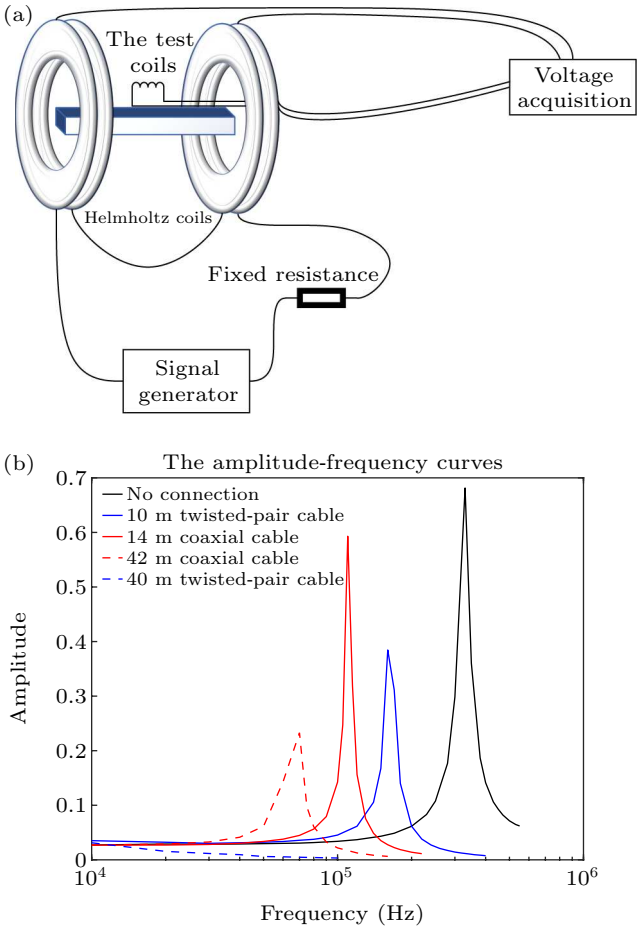


Fig. 8. (a) Helmholtz coil calibration diagram. (b) Amplitude–frequency curves.

In the entire signal acquisition circuit, long-distance cable transmission will lead to attenuation of the frequency response.[21] In this calibration, both a twisted-pair cable and a coaxial cable are tested. Figure 8 shows that the resonant frequency gradually decreases with increase in the length of the wire. Furthermore, it is found that the linear region of the amplitude–frequency curve is 50 kHz when 42 m of coaxial cable is connected to the circuit, and the resonance frequency is 70 kHz. When a 40 m twisted-pair wire is connected to the circuit, attenuation of the signal amplitude decreases more rapidly and a resonance frequency is not observed in this case. Therefore, coaxial cable is more conducive to high-frequency signal transmission than twisted pair cable. According to recent experiments, in HT-6M operation, the tearing mode is observed under ohmic heating and the frequency is about 20 kHz–40 kHz. Based on the previous platform test, to meet Thailand's 100 kHz frequency response requirements, a magnetic probe matched with 5 m coaxial cable is used.

Rogowski coil calibration In order to verify the previously calibrated mutual inductance of the Rogowski coil and ensure the accuracy of magnetic measurement, the coefficient of the Rogowski coil is checked. The Rogowski coil is calibrated through a circuit loop. The circuit current can be obtained by measuring the voltage across the high-power resistors in the circuit (red line in Fig. 9). Then a coil with a known number of turns ($N \cdot I$) is connected in series into the circuit, and the Rogowski coil is used to measure the current of the coil. The output voltage of the Rogowski coil is obtained. By inverse calculation of the output voltage of the Rogowski coil, a calculated value can be obtained. The error is found to be less than 1% compared with the standard current obtained from the resistor. Figure 9 compares the signal size curves obtained through inverse calculation. The red line is the standard current, and the blue line is the inverse calculated value.

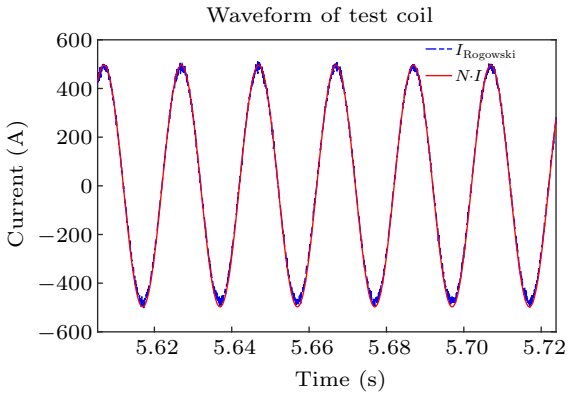


Fig. 9. Calibration diagram for a Rogowski coil.

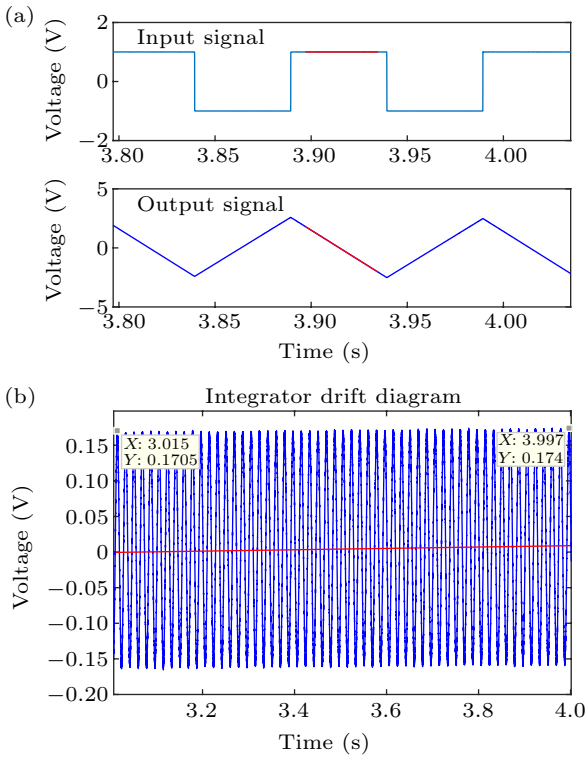


Fig. 10. Integrator calibration: (a) *RC* value calibration, (b) integrator drift.

Integrator constant calibration The time constant (*RC*) of the integrator is an important parameter of the integrator, and its precision will affect the precision of the system.[22] This calibration adopts the method of inputting a specific signal to the integrator and calculating the integral constant of the integrator through the amplitude of the output signal. The

input signal is a standard square-wave signal. As shown in Fig. 10, by inputting a standard square wave signal with an amplitude of 1 V to the integrator, the value of G/RC is then obtained from the average slope of the resulting triangle-wave output. The integral constant RC can be obtained from the formula

$$RC = \frac{V_{\text{in}}}{k_{\text{s}}}, \tag{15}$$

where k_{s} is the average slope of the resulting triangle-wave output and V_{in} is the input voltage.

The result shows that the integral constant error of the integrator is about 1.5%. In addition, the calibration analysis checks for noise and distortion in the output. The analysis shows that noise is less than 10 mV and drift is less than 5 mV·s^{-1}, as shown in Fig. 10(b).

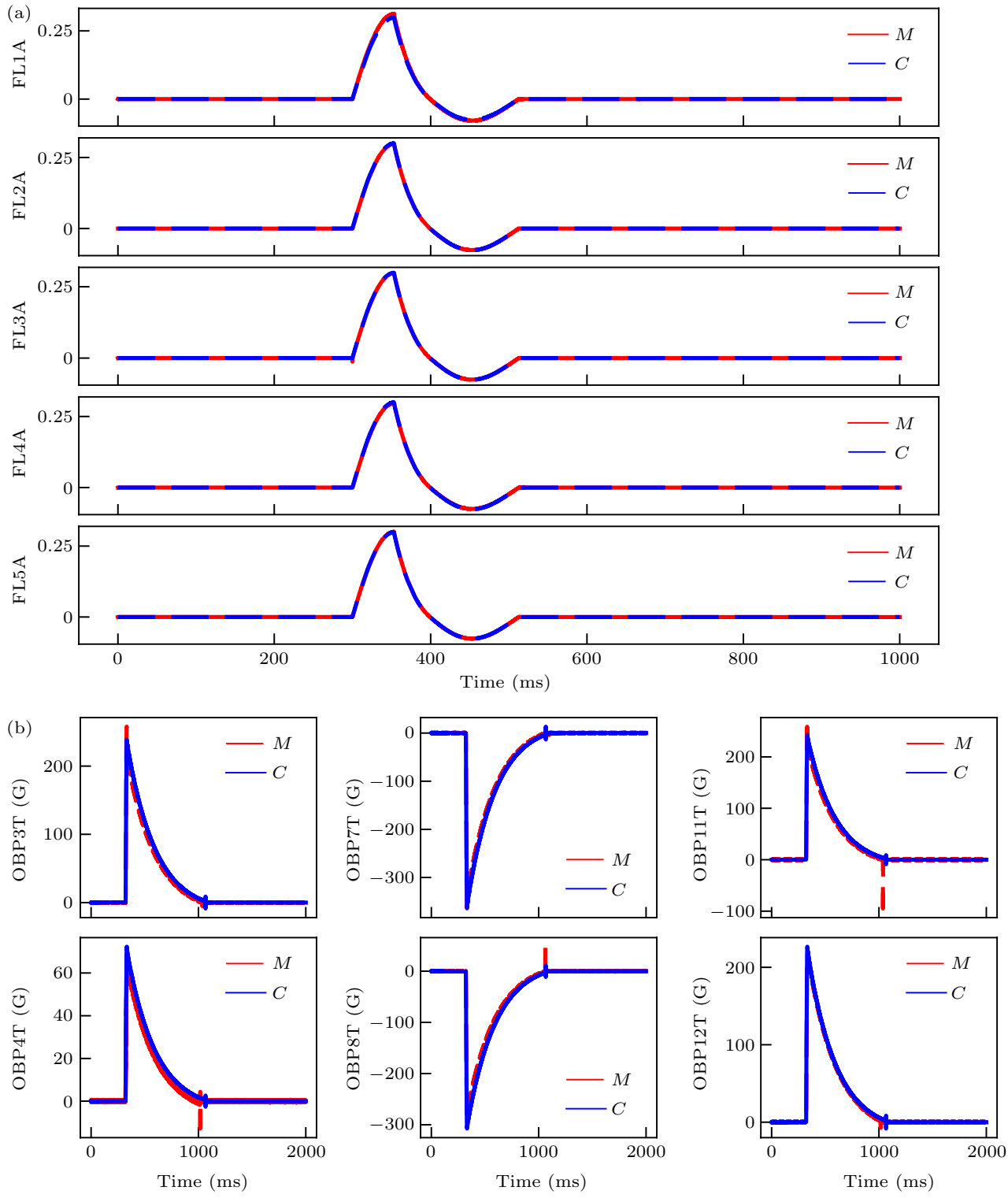


Fig. 11. Magnetic diagnostic calibration: (a) calculated and measured flux loops values, (b) calculated and measured magnetic probe values.

4.2. Experimental results for magnetic sensors

After calibration of the Rogowski coils, the current of the PF coil can be accurately measured. Then, the theoretical values for the magnetic probes and flux loops can be calculated by multiplying the measured coil current and response matrix between the PF coils and these diagnostics. The accuracy of the magnetic probe can be verified by comparing the calculated value with the measured value

$$\boldsymbol{B}_{\mathrm{p}} = \boldsymbol{G}_{\mathrm{CP}} \times I_{\mathrm{c}}, \tag{16}$$

where $\boldsymbol{B}_{\mathrm{p}}$ is the reconstructed poloidal field of the magnetic probe on the chamber, $\boldsymbol{G}$ is the response matrix between the OHF coils and magnetic diagnostics and I_{c} is the OHF coil current

$$\Phi_{\mathrm{p}} = \boldsymbol{G}_{\mathrm{CP}} \times I_{\mathrm{c}} \times NS_{\mathrm{FL}}, \tag{17}$$

where Φ_{p} is the reconstructed poloidal field of the flux loop on the chamber, $\boldsymbol{G}$ is the response matrix between the OHF coils and magnetic diagnostics, I_{c} is the OHF coils current and NS_{FL} is the flux loop coefficient.

Then, the calculated value for the magnetic field of the magnetic sensors can be obtained from Eqs. (16) and (17).

Figure 11 compares the measured and calculated values in a test discharge. In the 24 shots, the OHF coil current is 15.6 kA and the other coils have no current. Good consistency means perfect installation and calibration of the magnetic diagnostics system.

In order to verify the null field, a fitting code was developed to reconstruct the stray field in the vacuum chamber based on measured values for the magnetic probes and flux loops. The reconstructed OHF coil current can be acquired by least-squares fitting based on

$$I_{\mathrm{c}} = \boldsymbol{G}_{\mathrm{CD}}^{-1} \times D, \tag{18}$$

where I_{c} is the OHF coil current, $\boldsymbol{G}_{\mathrm{CD}}$ is the response matrix between OHF coils and the magnetic diagnostics and D is the measured value for the magnetic diagnostics.

After obtaining the OHF coil current, the poloidal field distribution in the vacuum chamber can be calculated by

$$\boldsymbol{B}_{\mathrm{p}} = \boldsymbol{G}_{\mathrm{CP}} \times I_{\mathrm{c}}, \tag{19}$$

where $\boldsymbol{B}_{\mathrm{p}}$ is the reconstructed poloidal field in the chamber, $\boldsymbol{G}_{\mathrm{CP}}$ is the response matrix between the OHF coils and calculated grids in the chamber. As shown in Fig. 12, a large region with a small stray field (< 10 G) can be achieved, which is consistent with the desired null field in the device optimization phase. A comparison of the measured and reconstructed OHF coils is shown in Fig. 11. Consistent results verify good null field optimization.

Figure 13 shows that the 20 G region basically covers the whole vacuum chamber during the period from 340 ms to 360 ms with an OHF coil current of only 15.6 kA, which is favorable for subsequent plasma breakdown.

The result shows that the error between the calculated electromagnetic measurement and the measured value is not large, basically $< 1.5\%$. It lays a solid foundation for the good discharge conditions in the experiments.

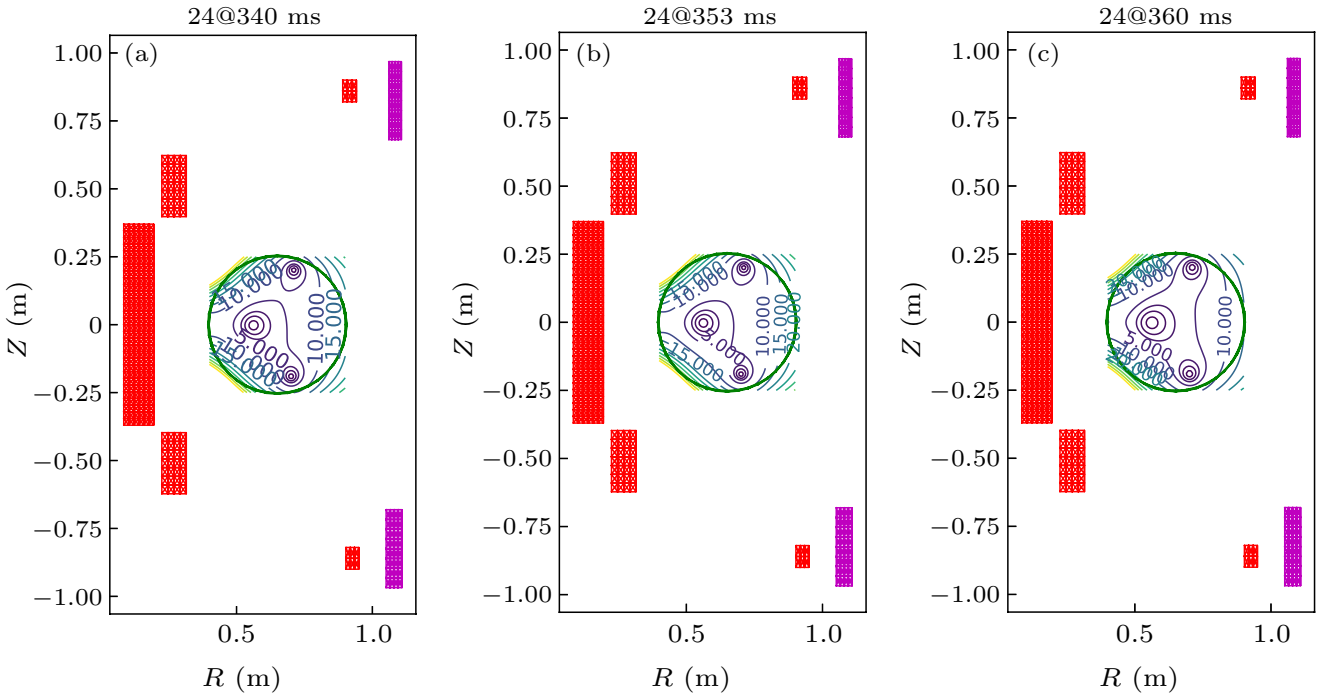


Fig. 12. Vacuum field configuration inversion.

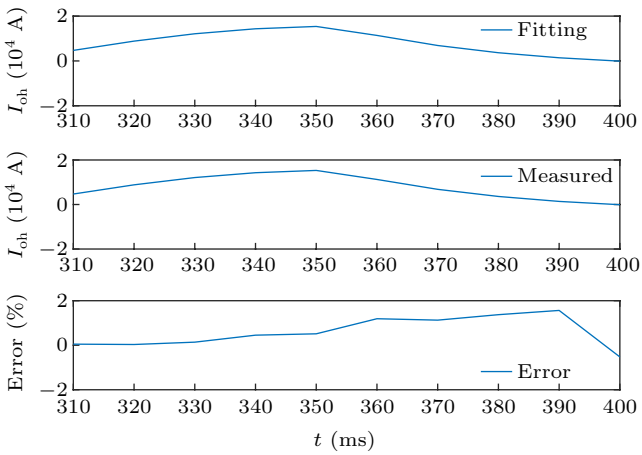


Fig. 13. The 24-shot calculated and measured values.

5. Summary

As an indispensable part of the tokamak diagnostic process, magnetic diagnostics are the most effective means to obtain device engineering parameters and internal plasma information by using the principle of electromagnetic induction. Its main functions are: (i) protection of device safety, (ii) provision of input parameters needed for device operation and real-time control, (iii) experimental physics studies of MHD behavior, plasma rupture physics and so on.

In this article, the original HT-6M device was first modeled and calculated. The previous device parameters could not meet the design requirements for perfect plasma zero field. The position of the ohmic field coils (OHF2U, OHF2L, OHF3U, OHF3L) was optimized, and a perfect zero field obtained. The third part involved designing an arrangement of magnetic probes including a Rogowski coil, flux loop ring, magnetic probe and diamagnetic coil. Finally, the calibration and experimental results of the magnetic probes are described: *NS* value, frequency response, integral constant (*RC*) of the integrator, zero drift and the calculated and measured values of the total experimental Green's function of the magnetic probe are compared. It is demonstrated that the measurements are in good agreement with the modelling, which indicates that the magnetic system works well. After the reconstruction of the vacuum field shape during the discharge test, it is found that a 20 G area basically covers the whole vacuum chamber, which is quite reasonable for subsequent plasma breakdown. Finally, by reconstructing the plasma equilibrium, a better PF coil comparison result is obtained, which can meet the discharge requirements. In recent experiments, the upgraded tokamak has shown a smooth breakdown with optimized null field, and a discharge above 50 kA for longer than 100 ms has been achieved.

Acknowledgments

The authors acknowledge Xueqin Li and Jun Wei for helpful discussions about the design of the magnetic probe.

Project supported by the National MCF Energy Research and Development Program of China (Grant Nos. 2018YFE0302100 and 2018YFE0301105), the National Natural Science Foundation of China (Grant No. 11875291), and the Comprehensive Research Facility for Fusion Technology Program of China (Grant No. 2018-000052-73-01-001228).

References

[1] Qing Y W 2011 2011 *Experimental Physics Foundations of the Tokamak* (1st Edn.) (Bei Jing: Atomic Energy Publishing House) p. 18
[2] Wang L 2018 2018 *Experimental Physical of Magnetic Confinement Plasmas* (1st Edn.) (Beijing: China Science Publishing & Media Ltd.) p. 81
[3] Shen B, Luo J R, Wan B N and Wang H Z 2003 *Plasma Sci. Technol.* **5** 1785
[4] Chen D L, Robert G, Shen B, Yang F, Qian J P and Xiao B J 2015 *Chin. Phys. B* **24** 025205
[5] Strait E J 2006 *Rev. Sci. Instrum.* **77** 023502
[6] Lao L L, John H S, Stambaugh R D, Kellman A G and Pfeiffer W 1985 *Nucl. Fusion* **25** 1611
[7] Luo Z P, Xiao B J, Zhu Y F and Yang F 2010 *Plasma Sci. Technol.* **12** 412
[8] Qian J P, Wan B N, Shen B, Lao L L, Xiao B J, Li J G, Lin S Y and Luo Z P 2009 *Chin. Phys. B* **18** 1172
[9] Qing Y W 2011 *Experimental Physics Foundations of the Tokamak* (1st Edn.) (Bei Jing: Atomic Energy Publishing House) p. 256
[10] Chen D L, Shen B, Qian J P, Sun Y W, Liu G J, Shi T H, Zhuang H D and Xiao B J 2014 *Chin. Phys. B* **23** 065205
[11] Liu G J, Wan B N, Sun Y W, Xiao B J, Wang Y, Luo Z P, Qian J P and Liu D M 2013 *Rev. Sci. Instrum.* **84** 073502
[12] Shen B, Wan B N and Zhang X Q 2004 *Fusion Eng. Des.* **70** 311
[13] Jia T Q, He K Y, Chen D L, Qian J P, Gu X, Shen B, Sun Y W, Shi T H, Wang Y, Zhang B and Gong X Z 2022 *Fusion Eng. Des.* **177** 113091
[14] Smyte W 1950 *Static and Dynamic Electricity* (2rd Edn.) (New York: McGraw-Hill) p. 48
[15] Equipe T F R 1978 *Nucl. Fusion* **18** 647
[16] Mukhovatov V S and Shafranov V D 1971 *Nucl. Fusion* **11** 605
[17] King J D, Strait E J, Boivin R L, Taussig D, Watkins M G, Hanson J M, Logan N C, Paz-Soldan C, Pace D C, Shiraki D, Lanctot M J, La Haye R J, Lao L L, Battaglia D J, Sontag A C, Haskey S R and Bak J G 2014 *Rev. Sci. Instrum.* **85** 083503
[18] Dai X J, Shen B and Liu G J 2010 *Nuclear Fusion and Plasma Physics* **30** 360 (in Chinese)
[19] Sun J Y, Shen B, Liu G J, Sun Y W, Qian J P, Li S, Xiao B J, Chen D L and Shi T H 2014 *Nuclear Fusion and Plasma Physics* **34** 265 (in Chinese)
[20] Strait E J 1996 *Rev. Sci. Instrum.* **67** 2538
[21] Dai X J, Shen B, Jiang L and Liu G J 2011 *Nuclear Fusion and Plasma Physics* **31** 5 (in Chinese)
[22] Wu Y C, Wang Y, Liu D M, Ji Z S and Luo J R 2009 *Atomic Energy Science and Technology* **43** 12
[23] Qian J P, Wan B N, Lao L L, Shen B, Sabbagh S A, Sun Y W, Liu D M, Xiao B J, Ren Q L and Luo J R 2009 *Plasma Sci. Technol.* **11** 142
[24] Liu G J, Wan B N, Sun Y W, Liu Y Q, Guo W F, Hao G Z, Ding S Y, Shen B, Xiao B J and Qian J P 2014 *Chin. Phys. B* **23** 075205